Astronomy & Astrophysics manuscript no. paper
February 7, 2022

Comparison of synthetic maps from truncated jet-formation models with YSO jet observations

II. The effect of varying inclinations

Matthias Stute[1] and José Gracia[2]

[1] Institute of Astronomy and Astrophysics, Section Computational Physics, Eberhard Karls Universität Tübingen, Auf der Morgenstelle 10, 72076 Tübingen, Germany
[2] High Performance Computing Center Stuttgart (HLRS), Universität Stuttgart, 70550 Stuttgart, Germany

Received ; accepted

ABSTRACT

Context. Analytical radially self-similar models are the best available solutions describing disk-winds but need several improvements. In a previous article, we introduced models of jets from truncated disks, i.e. evolved in time numerical simulations based on a radially self-similar MHD solution but including the effects of a finite radius of the jet-emitting disk and thus the outflow. In paper I of this series, we compared these models with available observational data varying the jet density and velocity, the mass of the protostar and the radius of the aforementioned truncation.
Aims. In paper I, we assumed that the jet lies in the plane of the sky. In this paper, we investigate the effect of different inclinations of the jet.
Methods. In order to compare our models with observed jet widths inferred from recent optical images taken with HST and AO, we create again emission maps in different forbidden lines and from such emission maps, we determine the jet width as the full-width half-maximum of the emission.
Results. We can reproduce the jet width of DG Tau and its variations very well and the derived inclination of 40° is in excellent agreement with literature values of 32–52°. In CW Tau we overestimate the inclination in our best-fit model. In the other objects, we cannot find appropriate models which reproduce the variations of the observed jet widths, only the average jet width itself is well modeled as in paper I.
Conclusions. We conclude that truncation – i.e. taking into account the finite radius of the jet launching region – is necessary to reproduce the observed jet widths and our simulations limit the possible range of truncation radii. The effects of inclination are important for modeling the intrinsic variations seen in observed jet widths. Our models can be used to infer independently the inclinations in the observed sample, however, a parameter study with a finer grid of parameters is needed.

Key words. MHD — methods: numerical — ISM: jets and outflows — Stars: pre-main sequence, formation

1. Introduction

Astrophysical jets and disks (Livio 2009) seem to be interrelated, notably in the case of young stellar objects (YSOs), wherein jet signatures are well correlated with the infrared excess and accretion rate of the circumstellar disk (Cabrit et al. 1990; Hartigan et al. 2004). Disks provide the plasma which is outflowing in the jets, while jets in turn provide the disk with the needed angular momentum removal in order that accretion in the protostellar object takes place (Hartmann 2009). On the theoretical front, the most widely accepted description of this accretion-ejection phenomenon (Ferreira 2007) is based on the interaction of a large scale magnetic field with an accretion disk around the central object. Then, plasma is channeled and magneto-centrifugally accelerated along the open magnetic field lines threading the accretion disk, as firstly described in Blandford & Payne (1982). Several works have extended this study either by semi-analytic models using radially self-similar solutions of the full magnetohydrodynamics (MHD) equations with the disk treated as a boundary condition (Vlahakis & Tsinganos 1998), or, by selfconsistently treating numerically the disk-jet system (e.g. Zanni et al. 2007).

The original Blandford & Payne (1982) model, however, has serious limitations for a needed meaningful comparison of its predictions with observations. Singularities exist at the jet axis, the outflow is not asymptotically superfast, and most importantly, the disk has no intrinsic scale with the result that the jet formally extends to radial infinity, to mention just a few. The singularity at the axis can be easily taken care of by numerical simulations extending the analytical solutions close to this symmetry axis (Gracia et al. 2006, GVT06 hereafter). The outflow speed at large distances may be tuned to cross the corresponding limiting characteristic, with the result that the terminal wind solution is causally disconnected from the disk and hence perturbations downstream of the superfast transition (as modified by self-similarity) cannot affect the whole structure of the steady disk-wind outflow (Vlahakis et al. 2000, V00 hereafter) which has also been shown to be structurally stable (Matsakos et al. 2008, M08 hereafter). The next step of introducing a scale in the disk has been undertaken in a previous paper (Stute et al. 2008), wherein we presented numerical simulations of truncated flows whose initial conditions are based on analytical self-similar models.

Send offprint requests to: Matthias Stute,
e-mail: matthias.stute@tat.physik.uni-tuebingen.de

In order to test our truncated models, we then applied our simulations to observations (Stute et al. 2010, paper I hereafter). In recent years, many NIR and optical data have become available exploring the morphology and kinematics of the jet launching region (e.g. Dougados et al. 2000; Ray et al. 2007; Dougados 2008, and references therein). HST and adaptive optics observations give access to the innermost regions of the wind, where the acceleration and collimation occurs (Ray et al. 1996; Dougados et al. 2000; Woitas et al. 2002; Hartigan et al. 2004). Since YSO jets emit in a number of atomic (and molecular) lines, we use a synthetic emission code to create emission maps in different forbidden lines which were used by other authors to extract the jet width from images. In paper I, we compared the observed jet widths with those extracted from our synthetic images. A similar study has been done by Ferreira (1997); Casse & Ferreira (2000); Garcia et al. (2001); Dougados et al. (2004), however, using untruncated disk wind models.

In paper I, however, we always assumed the inclination of the jet to be 90°. The influence of varying inclinations on the derived synthetic jet widths will be examined now in this paper.

The remainder of the paper is organized as follows: we briefly review the initial set-up of the numerical simulations and describe our procedure for the comparison with observations in Sec. 2. The results of our studies are presented in Sec. 3. In Sec. 4 we describe our best-fit models for each object in the sample and compare derived inclinations with literature values. Finally, we conclude with the implications of the results in terms of the structure of the disk and the respective launching radii of the jets in YSOs. In appendix A, we present the extracted line widths for all models, runs and inclinations for the sake of completeness. Jet velocities derived from synthetic position- velocity diagrams are given in Appendix B.

2. The models

2.1. Initial set-up and numerical simulations

This work is based on the results of our numerical simulations discussed in Stute et al. (2008) and two new models already added in paper I (Table 1). We solved the MHD equations with the PLUTO code[1] (Mignone et al. 2007) starting from initial conditions set according to a steady, radially self-similar solution as described in V00 which crosses all three critical surfaces. At the symmetry axis, the analytical solution was modified as described in GVT06 and M08.

To study the influence of the truncation of the analytical solution, we divide our computational domain up into a jet region and an external region, separated by a truncation field line $\alpha_{\rm trunc}$. For lower values of the normalized magnetic flux function, i.e. $\alpha < \alpha_{\rm trunc}$ – or conversely smaller cylindrical radii – our initial conditions are fully determined by the solution of V00 and the modification of GVT06 and M08 close to the axis. In the outer region, we modify all quantities and initialize them with another analytical solution but with modified parameters (models with outer truncation; SC1a–g, SC2, SC4). In models SC1a–g we varied the truncation radius and within models SC1a, SC2 and SC4, we probed different modifications in the outer region. Two simulations have been performed with inner truncation (SC3, SC5), i.e. the analytical solution with modified quantities is inside the original analytical solution. For further details, we refer the reader to Stute et al. (2008).

[1] http://plutocode.to.astro.it/

2.2. Synthetic emission maps and jet width extraction

We use the synthetic emission code OpenSESAMe v0.1 to produce synthetic observations from our simulations in different consecutive stages. The first stage approximates the chemical composition of the plasma by locally solving a chemical network under the assumption of stationarity. The second stage calculates the statistical equilibrium of level populations for each ion of interest as a function of temperature and density and yields the emissivity for individual transitions of interest. Further stages take care of integration along the line-of-sight and projection. Finally, the ideal maps are convolved with a Gaussian point-spread-function (PSF) to mimic the finite spatial resolution of a given instrument. These synthetic emission maps are then quantitatively analysed with similar techniques used on real observed maps.

We compare the width of jets measured from HST and AO observations (Dougados et al. 2000; Ray et al. 2007; Dougados 2008, and references therein) to synthetic emission maps calculated from our MHD models. We convolved the maps with a Gaussian with a FHWM of 15 AU (σ = 6.37 AU) throughout this paper, equivalent to HST's resolution of 0.1" at a distance of 150 pc. We use a sample of eight jets: DG Tau, HN Tau, CW Tau, UZ Tau E, RW Aur, HH34, HH30 and HL Tau (Fig. 1). In order to determine the width of the jets in our models, we use a method which is as close as possible to that applied by the observers. We create convolved synthetic maps for the emission in the [SII] λ6731 and [OI] λ6300 lines for each numerical model and each run of OpenSESAMe and determine the jet width from the map's full-width half-maximum (FWHM) as a function of distance along the axis.

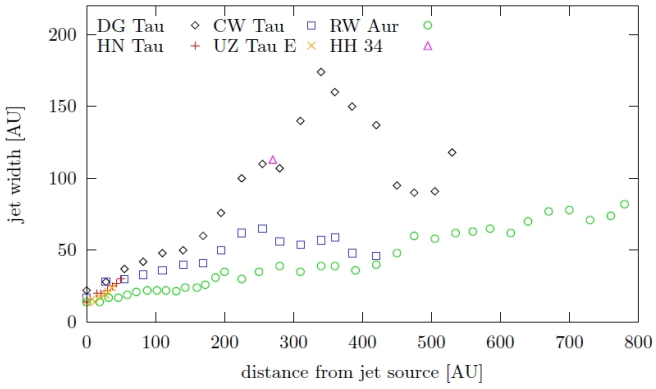

Fig. 1. Variation of jet width (FWHM) derived from [SII] and [OI] images as a function of distance from the source. Data points are from CFHT/PUEO and HST/STIS observations of DG Tau (diamonds), HN Tau (plus signs), CW Tau (squares), UZ Tau E (crosses), RW Aur (circles), HH 34 (one triangle); data are taken from Ray et al. (2007) for distances below 200 AU and Dougados et al. (2000) beyond this distance.

2.3. Normalizations

In order to compare our results with observations, i.e. in order to run OpenSESAMe correctly, we have to scale the dimensionless quantities in which PLUTO performs its calculations (Stute et al. 2008) to physical units by providing scaling factors for density ρ_0, pressure p_0, velocity v_0, magnetic field strength B_0, a length scale R_0 and a mass scale $\mathcal{M}$. However, in terms of the normal-

Table 1. List of numerical models

Name	$R_{\rm trunc}$ [R_0]	Description
model ADO	∞	unchanged analytical solution of V00
model SC1a	5.375	analytical solution is truncated for $R > R_{\rm trunc}$ (outer truncation), quantities are scaled down by factors of $10^{-6...-1.5}$
model SC1b	5.125	same as model SC1a, but different $R_{\rm trunc}$
model SC1c	4.875	same as model SC1a, but different $R_{\rm trunc}$
model SC1d	3.625	same as model SC1a, but different $R_{\rm trunc}$
model SC1e	2.625	same as model SC1a, but different $R_{\rm trunc}$
model SC1f	2.375	same as model SC1a, but different $R_{\rm trunc}$
model SC1g	0.575	same as model SC1a, but different $R_{\rm trunc}$
model SC2	5.375	analytical solution is truncated for $R > R_{\rm trunc}$ (outer truncation), scale factors of $10^{-2...-1}$, density unchanged
model SC3	5.375	same as model SC2, but analytical solution is truncated for $R < R_{\rm trunc}$ (inner truncation)
model SC4	5.375	analytical solution is truncated for $R > R_{\rm trunc}$ (outer truncation), scale factors of $10^{-2...-1}$, velocity unchanged

For further details, we refer the reader to Stute et al. (2008). The meaning of R_0 is described in Sec. 2.3.

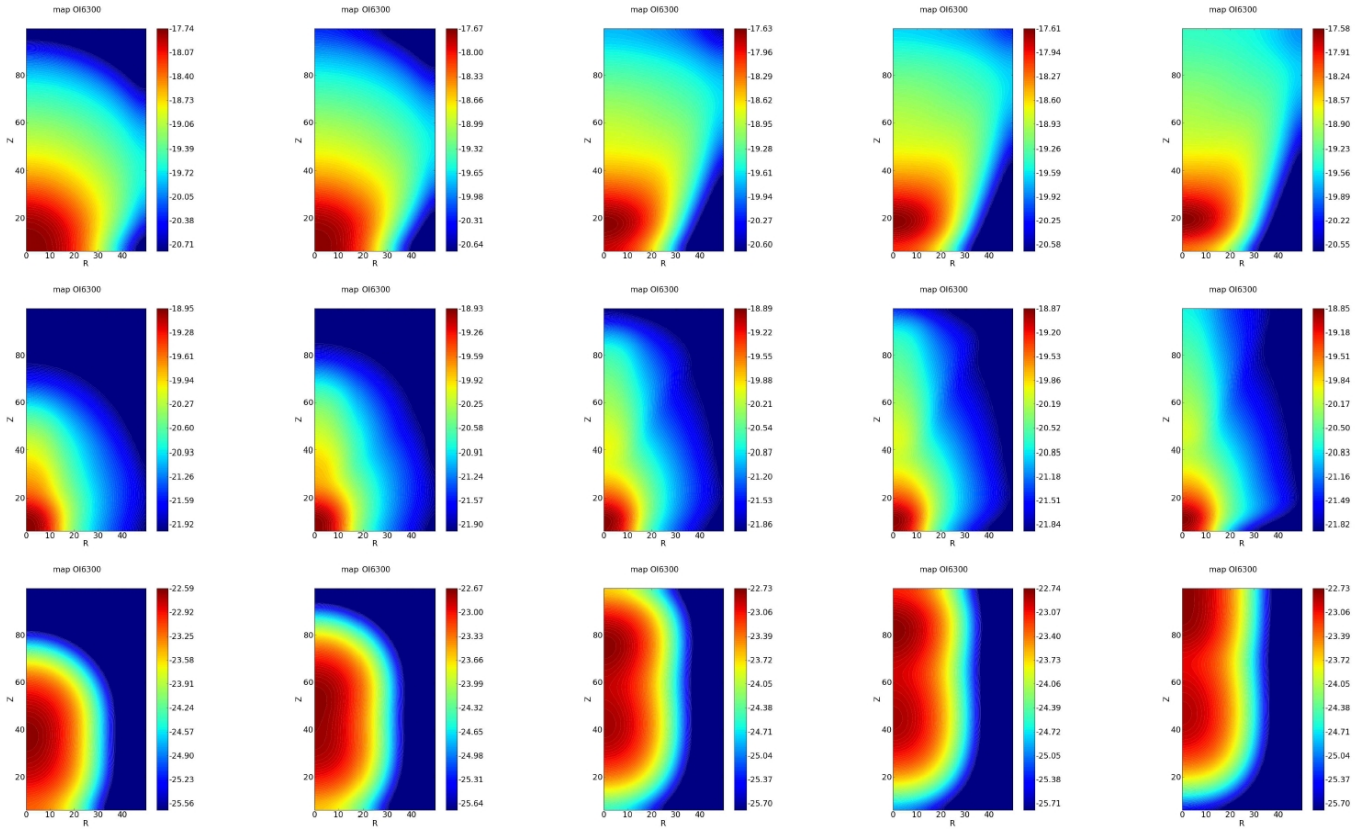

Fig. 2. Synthetic emission maps of the [OI] λ6300 line, convolved with a Gaussian PSF with a FWHM of 15 AU, for run (500,1000,0.5) and the untruncated model ADO (top) and the model SC1a with outer truncation (middle) and for run (500,100,0.2) and model SC3 with inner truncation (bottom). The inclinations are 30°, 40°, 60°, 70° and 90° (from left to right). The flux is in units of erg s^{-1} cm^{-2}.

izations used in the PLUTO code, only three of those quantities are indepedent. A possible choice is the mass of the central object, velocity scale and density scale, while the remaining factors are calculated from these. The PLUTO domain is set from (0,6) to (50,100) and the physical scale of the jet in AU is simply the PLUTO domain multiplied with a length scale R_0. In the solution of V00, the length scale R_0 is connected to the mass of the central object and the velocity normalization via

$$R_0 = \frac{\mathcal{G}\,\mathcal{M}}{4\,v_0^2} = 110.9\,\mathrm{AU}\left(\frac{v_0}{\mathrm{km\ s^{-1}}}\right)^{-2}\left(\frac{\mathcal{M}}{0.5\,\mathrm{M_\odot}}\right). \quad (1)$$

From the velocity and density normalization directly follow the normalizations for the magnetic field and pressure as

$$p_0 = \rho_0\,v_0^2 = 10^{-11}\,\mathrm{g\ cm^{-1}\ s^{-2}}\left(\frac{\rho_0}{10^{-21}\,\mathrm{g\ cm^{-3}}}\right)\left(\frac{v_0}{\mathrm{km\ s^{-1}}}\right)^2, \quad (2)$$

$$B_0 = \sqrt{4\,\pi\,\rho_0\,v_0^2} = 11.21\,\mu\mathrm{G}\left(\frac{\rho_0}{10^{-21}\,\mathrm{g\ cm^{-3}}}\right)^{1/2}\left(\frac{v_0}{\mathrm{km\ s^{-1}}}\right). \quad (3)$$

The mass of the central object affects only the length scale R_0. The pressure and temperature of the jet, and thus the synthetic emission maps, are affected only by the density and velocity scales ρ_0 and v_0.

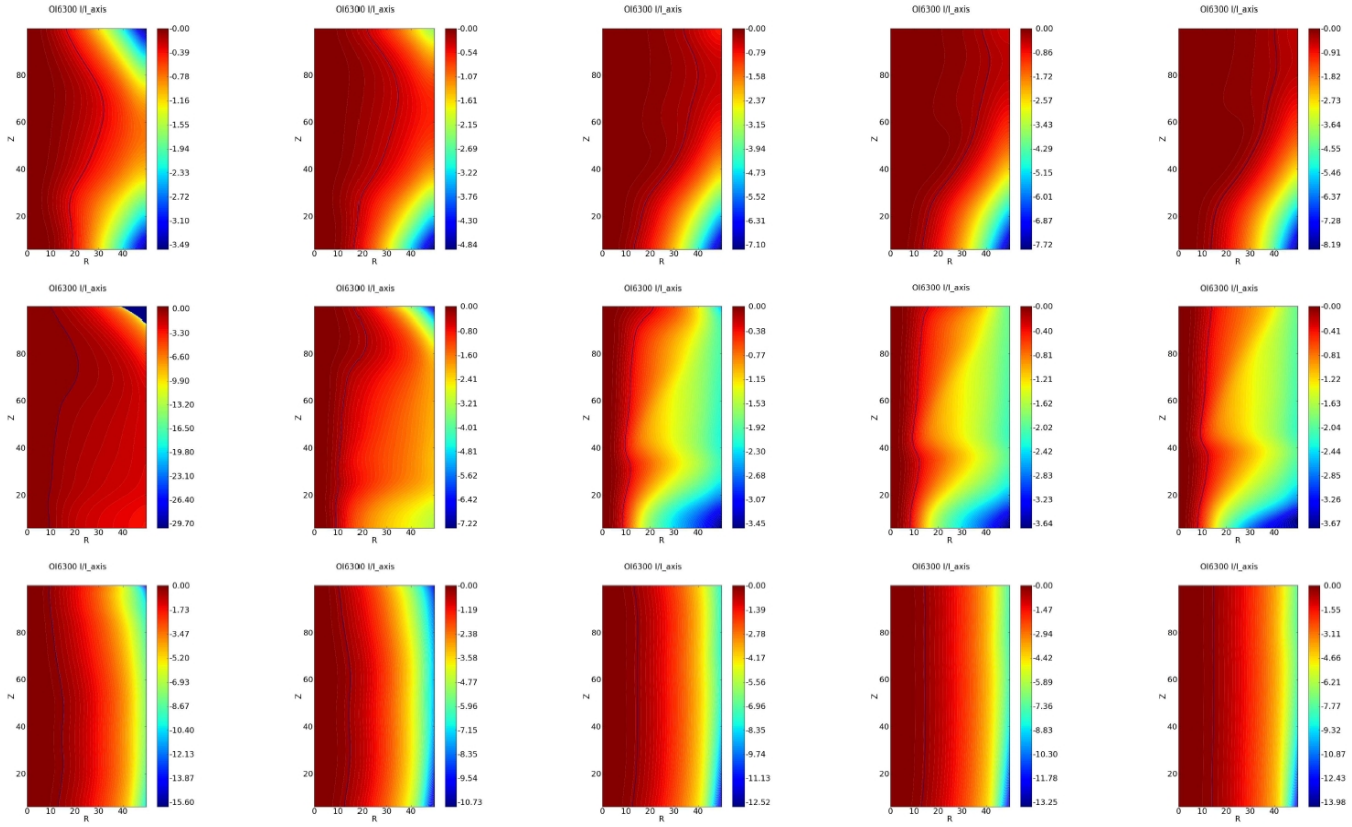

Fig. 3. same as Fig. 2, however, normalized by the intensity on the jet axis for each row; also plotted is the contour line where $I/I_{\rm axis} = 0.5$, i.e. the position of the FWHM.

As typical jet velocities in YSOs, we assumed in paper I values of 100, 300, 600 and 1000 km s^{-1}, as typical masses of T Tauri stars 0.2, 0.5 and 0.8 $M_\odot$ (Hartigan et al. 1995), and as jet number densities values of 125, 500, 1000 and 5×10^4 cm^{-3}. We adopt the nomenclature for our runs as e.g. (500,600,0.5) with $n_{\rm jet}$ in cm^{-3}, $v_{\rm jet}$ in km s^{-1} and M in $M_\odot$.

For numerical reasons, the density shows a steap increase close to the jet axis. This artefact had to be corrected, therefore we applied the following corrections before running OpenSESAMe, as in paper I. We limit the temperature to 10^4 K, the density around the axis by setting the density inside 1 FWHM to its value at 1 FHWM for each z and the fraction $x_{\rm e} = n_{\rm e}/n_{\rm tot}$ to 0.1. These values of $x_{\rm e}$ and T are typical of those deduced from analyses of line ratios in jets (e.g. Bacciotti & Eislöffel 1999; Lavalley-Fouquet et al. 2000).

With the same requirement that the FWHM of the Gaussian of 15 AU is sampled by a reasonable number of pixels (see paper I), the only valid runs are

- (···,600,0.2), (···,600,0.5), (···,1000,0.5), (···,1000,0.8) for models ADO, SC1a–b, SC2, SC4
- (···,600,0.2), (···,600,0.5), (···,1000,0.2), (···,1000,0.5), (···,1000,0.8) for models SC1c–f
- (···,600,0.2), (···,1000,0.2), (···,1000,0.5), (···,1000,0.8) for model SC1g
- (···,100,0.2) for model SC3
- no valid runs for model SC5.

At first sight, the required velocities of 600 and 1000 km s^{-1} in our models with outer truncation SC1a–g, SC2 and SC4 seem to be chosen too high in comparison with observed values in typical YSO jets. We have to note that the velocity $v_{\rm jet}$ is a formal parameter of the model and corresponds to a physical velocity component only very close to the source, i.e. is not the asymptotic velocity of the flow.

The observed velocities of YSO jets are usually inferred from either proper motions of jet knots (i.e. pattern speeds, not flow speeds) or position-velocity diagrams which show the velocities along the line of sight convolved with emissivity. In our simulations, proper motions cannot be measured due to missing patterns. In Fig. 4, we show a synthetic position-velocity diagram for model SC1a, run (500,1000,0.8) and an inclination of 40° – which will be our best-fit model for DG Tau – and the observed map of DG Tau from Lavalley-Fouquet et al. (2000). We chose a velocity resolution as in the observations, also the dynamical range is similar in both plots. We can directly see that large velocities around $v_{\rm jet}$ are detectable only close to the jet source, the velocity of the jet at distances larger than 0.5" is 220 km s^{-1} and thus in the range of the observed value of 280 km s^{-1}. In Appendix B, we list the velocities of the jet for most of our models derived from the synthetic position-velocity diagrams.

3. Results

Naturally the inclination plays a crucial role for the way how the jet is seen in synthetic emission maps. This is even more pronounced in the truncated jet solutions (Fig. 2).

3.1. Synthetic jet widths

We extracted the jet width from a *ratio* of intensities by using the FWHM, i.e. we divided the maps by the intensity on the axis

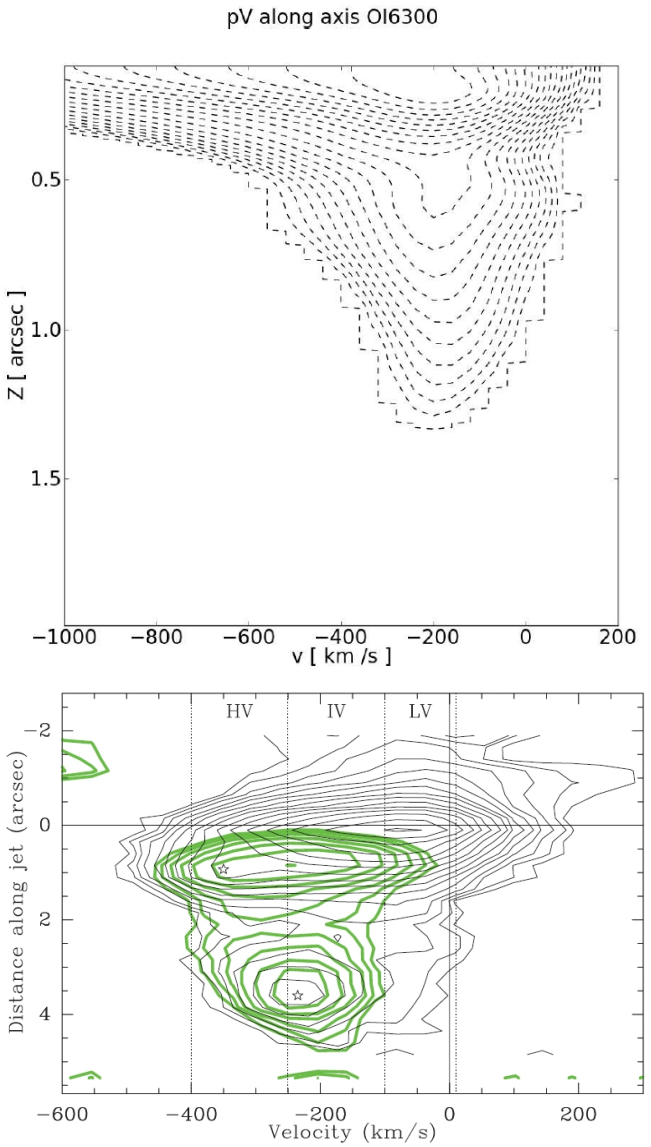

Fig. 4. Top: synthetic position-velocity diagram of the [OI] λ6300 line for model SC1a, run (500,1000,0.8) and an inclination of 40°, where we assumed a distance to the jet of 150 pc; bottom: observed position-velocity map of DG Tau for [OI] λ6300 (black thin lines) and [NII] λ6583 (green thick lines) from Lavalley-Fouquet et al. (2000). The dynamical range is similar in both plots. The velocity of the jet at distances larger than 0.5" in the model is 220 km s^{-1} and thus in the range of the observed value of 280 km s^{-1}.

and checked where the ratio is 0.5. Since in all models we have densities below the critical density the emissivity is proportional to ρ^2 in the whole domain, therefore the factor ρ^2 should cancel out. In paper I, we already found this behavior, the absolute value of the jet density is not important for the extracted jet widths. The same is present in this study, thus we will show mainly results with a jet density of 500 cm^{-3} throughout this paper.

A second result is the fact that the setup of the external solution is not important, i.e. the extracted jet widths of models SC1a, SC2 and SC4 are very similar. The only important parameters for our study are indeed the truncation radius and the inclination, when the jet velocity and mass of the central object are fixed by observations.

In paper I, we found that all untruncated ADO models give too large jet widths compared to the observations of T Tauri jets. This result is not changed when varying the inclination. We again conclude that we need an additional effect which reduces the derived jet width, in order to be able to reproduce all jets in our sample.

In paper I, we already found that the extracted jet width does not follow any directly apparent feature in neither the density or temperature map nor the emissivity map. A property of the extracted jet width, which was and still is intrinsic in all our runs, is the overall structure with at least one maximum. The position of maxima is generally only obvious in the normalized emission maps, i.e. after dividing by the intensity on the jet axis (Fig. 3). In paper I, we ignored this maximum and compared the synthetic jet widths with the observed ones only for large distances along the jet axis. Since the observed jet widths, however, also show a bumpy profile, it may be worth to further investigate the origin of the maxima in our simulations and to take them into account for fitting the observations.

The distance of the first maximum from the jet source increases for increasing mass of the central object and decreasing velocity of the jet. It also increases for increasing degree of truncation. In several models, a second maximum appears whose distance decreases for increasing degree of truncation.

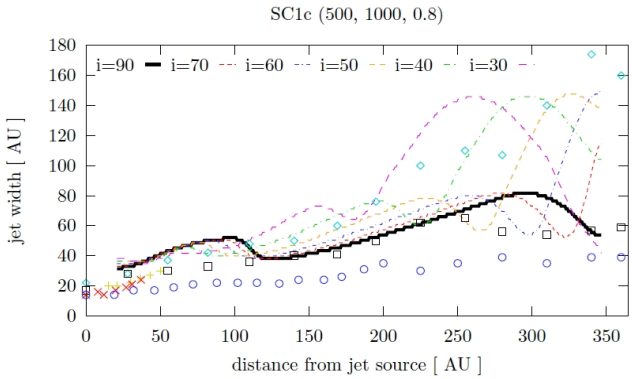

Fig. 5. Jet widths in AU derived from synthetic [OI] images as a function of distance from the source in model SC1c and for run (500,1000,0.8); overlaid are the data points of Fig. 1.

In the model SC3 with inner truncation, the derived jet width is almost constant. The effects of varying inclination are therefore only marginal when ignoring the geometrical effect mentioned above (Fig. 6).

3.2. On the origin of variations in the extracted jet widths

The fact that maxima were already present in our runs in paper I, i.e. in those with an inclination of 90°, shows that we have to differentiate between intrinsic variations and variations due to geometrical effects. First, we have to note again that maxima in the extracted jet width are not necessarily connected with e.g. density knots. In Stute et al. (2008), we found that the model with inner truncation SC3 collapses toward the jet axis leading to knots in the density maps. In paper I and also in Fig. 2 (bottom), we find in the corresponding synthetic emission map in [OI] two areas of enhanced emission whose position, however, is not the same as that of the density knots. Furthermore the extracted jet width is almost constant despite of these areas.

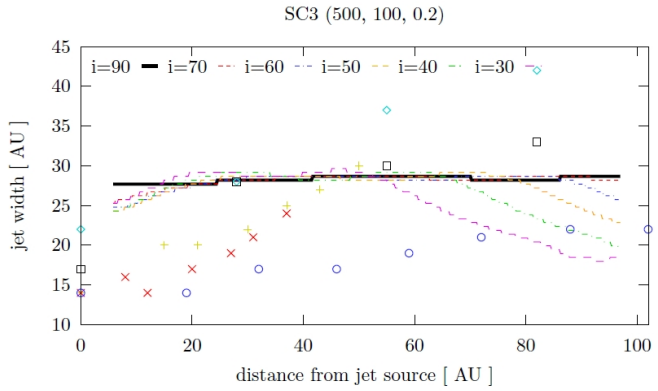

Fig. 6. Jet widths in AU derived from synthetic [OI] images as a function of distance from the source in model SC3 and for run (500,100,0.2); overlaid are the data points of Fig. 1.

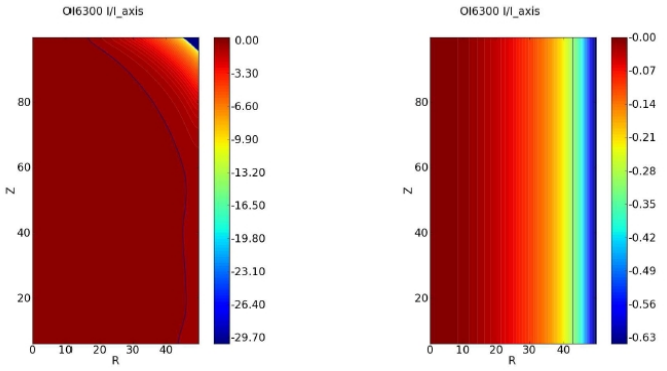

Fig. 7. Normalized emission map of the [OI] λ6300 line for a computational domain with constant density and temperature, the inclination is 40° (left) and 90° (right); also plotted is the contour line where $I/I_{\rm axis} = 0.5$, i.e. the position of the FWHM.

In order to find an physical origin of the variations, it is useful not to focus on the first maximum but on the minimum directly behind it. One common feature in all our MHD simulations is the fast magnetosonic separatrix surface (FMSS, Stute et al. 2008). This surface is a weak shock causally disconnecting the sub-fast flow from the super-fast one. Its position in Z direction increases monotonically with increasing R value. Both density and pressure along the flow line show a jump at the FMSS. As mentioned above, we convolve our map with a Gaussian of 15 AU and modify the density inside 15 AU from the jet axis. We find that the minimum in the extracted jet width is at the same position, where the FMSS has a radius of 15 AU and enters this region. For inclinations different to 90°, the two crossing points of FMSS with the Gaussian both in front of the jet and behind the jet are visible as local minima in the extracted jet widths.

Beyond physical origins of the maxima, another origin is the geometry of the system, i.e. the finiteness of our computational domain. In order to quantify this aspect, we calculated the emission maps and extracted jet width for a domain with constant density and temperature. Thus also the emission is constant across the domain. If seen with an inclination of 90°, the extracted jet width is constant as expected; if the inclination is 40°, however, the extracted jet width is almost constant only between about 15 and 68 R_0 (Fig. 7). These values are dependent on the aspect ratio of the computational domain and the tangent of the inclination. In our models, this geometrical effect leads to another maximum in extracted jet widths whose position moves to smaller distances with decreasing inclination (Fig. 5) and has to be corrected when comparing our models to observations. We used this test case with constant emission for quantifying the area in which our extracted jet widths are not affected by this effect.

4. Best-fit models

In paper I, we found best-fit models for the jets in the observed sample. Note that we always ignored there the first maximum in the synthetic jet widths and focussed on larger distances from the source. Now we can include the effects of inclination, use the position of the maxima in our synthetical jet width variations for estimating the inclination and compare the derived inclination with values from the literature.

4.1. DG Tau

The observed mass of DG Tau (diamonds in Fig. 1) is 0.67 $M_\odot$ (Hartigan et al. 1995), therefore we have to focus on the runs (500,1000,0.8), and perhaps also runs (500,600,0.5) and (500,1000,0.5). The best-fit model is between ADO and SC1a, thus the truncation radius is larger than 0.22 AU. DG Tau can be quite well reproduced with the model SC1a, the run (500,1000,0.8) and an inclination of 40° (Fig. 8). This inclination is in excellent agreement with the literature values of 32–52° (Eislöffel & Mundt 1998; Bacciotti et al. 2002; Pyo et al. 2003).

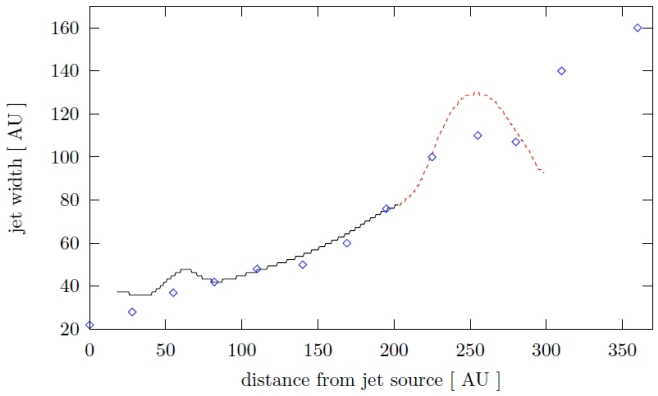

Fig. 8. Best-fit model for DG Tau: model SC1a, run (500,1000,0.8) and inclination of 40°. The red part is not reliable due to the geometric effect discussed in Sec. 3.2.

4.2. CW Tau

The mass of CW Tau (squares) is the highest in our sample, 1.03 $M_\odot$ (Hartigan et al. 1995). Using the runs (500,1000,0.8), the best-fit model was SC1b or SC1c. The truncation radius is thus between 0.25 – 0.3 AU. CW Tau may be best-modeled with simulation SC1c, run (500,1000,0.8) and an inclination of 60° (Fig. 9). The literature value, however, is about 41° (Coffey et al. 2007).

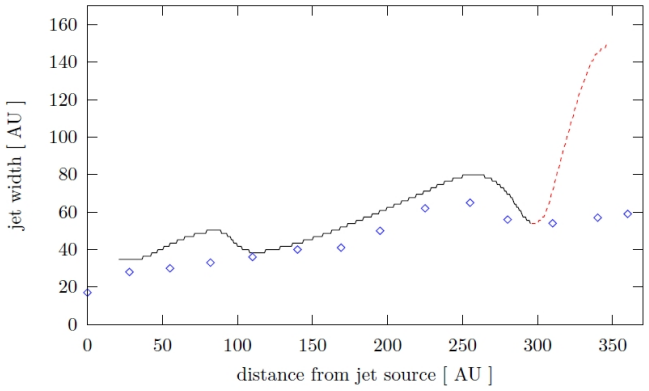

Fig. 9. Best-fit model for CW Tau: model SC1c, run (500,1000,0.8) and inclination of 60°. The red part is not reliable due to the geometric effect discussed in Sec. 3.2.

4.3. RW Aur

The measured mass of RW Aur (circles) is 0.85 $M_\odot$ (Hartigan et al. 1995), thus we had to focus on runs (500,1000,0.8). We needed a very high degree of truncation as in models SC1e-g, thus a truncation radius of the order of 0.04 AU, which seems to be unphysical. For these models, however, the influence of inclination is only marginal; we find literature values of 42° (Lay et al. 1997).

4.4. HN Tau and UZ Tau E

HN Tau (plus signs) has a mass of 0.72 $M_\odot$ (Hartigan et al. 1995), thus again the runs (500,1000,0.8) were favored. When we ignore the first maximum, we can interpolate the jet shape at larger distances and find a best-fit model between ADO and SC1a, thus the truncation radius is again larger than 0.34 AU. However, this result is highly uncertain and this procedure contradicts our present approach of taking the maxima into account.

UZ Tau E (crosses) has the lowest mass in our sample, only 0.18 $M_\odot$ (Hartigan et al. 1995), thus we used the runs (500,600,0.2). Again we have to interpolate the jet width from larger distances and could in principle choose model SC1a as best-fit model. The truncation radius would be about 0.26 AU.

Over all, we cannot find best-fit models, since our numerical resolution very close to the jet source is not sufficient enough; the inclination of HN Tau is not known (Hartigan et al. 2004), for that of UZ Tau E we find literature values of 60–70° (Jensen et al. 1996; Prato et al. 2002).

5. Summary and conclusions

In paper I, we showed as a proof of concept that jet widths derived from numerical simulations extending analytical MHD jet formation models can be very helpful for understanding recently observed jet widths from observations with adaptive optics and space telescopes. Here we investigated qualitatively the influence of different inclinations.

We examined the origin of variations in the extracted jet widths and identified physical and geometrical effects. We showed in which range our results are reliable and not affected by numerical artefacts.

We found that the distance of the first maximum from the jet source increases for increasing mass of the central object and decreasing velocity of the jet. It also increases for increasing degree of truncation. In several models, a second maximum appears whose distance decreases for increasing degree of truncation. The most noticeable effect of a decreasing inclination is a change in the position of the maxima in the synthetic jet widths. In all cases, the distance of the first maximum from the jet source decreases for decreasing inclination. The lower the inclination, the higher is also the number of maxima in the jet width.

We compared our synthetic jet widths with observations of our sample including the position of maxima in the jet width variations as diagnostics for the inclination. Only for DG Tau and CW Tau, we could unambiguously find models which fitted the observed jet widths. For the former, the derived inclination is perfectly consistent with values found in the literature; for the latter our derived inclination is higher than commonly measured (60° compared to 41°).

In a future work, we have to refine our grid of models for reproducing the observed jet widths and their variations even more accurate. These models have to be done with higher numerical resolution in order to give significant results in terms of synthetic emission maps even within a few AU to the jet source. Furthermore we have to extend the dimensions of our computational domain in order to avoid the described geometrical artefacts.

Acknowledgements. The authors would like to thank the referee for suggestions and comments which improved this paper.

References

Anderson, J. M., Li, Z.-Y., Krasnopolsky, R., Blandford, R. D. 2003, ApJ, 590, L107
Bacciotti, F., Eislöffel, J. 1999, A & A, 342, 717
Bacciotti, F., Ray, T. P., Mundt, R., et al. 2002, ApJ, 576, 222
Blandford, R. D., Payne, D. G. 1982, MNRAS, 199, 883
Cabrit, S., Edwards, S., Strom, S. E., Strom, K. M. 1990, ApJ, 354, 687
Casse, F., Ferreira, J. 2000, A & A, 353, 1115
Coffey, D., Bacciotti, F., Ray, T. P., et al. 2007, ApJ, 663, 350
Combet, C., Ferreira, J. 2008, A & A, 479, 481
Dougados, C., Cabrit, S., Lavalley, C., Menard, F. 2000, A&A, 357, L61
Dougados, C., Cabrit, S., Ferreira, J., Pesenti, N., Garcia, P., O'Brien, D. 2004, Ap & SS, 293, 45
Dougados, C. 2008, in: "Jets from Young Stars II: Clues from High Angular Resolution Observations", Lecture Notes in Physics, Vol. 742, F. Bacciotti, E. Whelan, L. Testi (Eds.), Springer-Verlag Berlin Heidelberg
Eislöffel, J., Mundt, R. 1998, AJ, 115, 1554
Ferreira, J. 1997, A & A, 319, 340
Ferreira, J. 2007, in: "Jets from Young Stars: Models and Constraints", Lecture Notes in Physics, Vol. 723, J. Ferreira, C. Dougados, E. Whelan (Eds.), Springer-Verlag Berlin Heidelberg
Garcia, P.J.V., Cabrit, S., Ferreira, J., Binette, L. 2001, A & A, 377, 609
Gracia, J., Vlahakis, N., Tsinganos, K. 2006, MNRAS, 367, 201, GVT06
Hartigan, P., Edwards, S., Ghandour, L. 1995, ApJ, 452, 736
Hartigan, P., Edwards, S., Pierson, R. 2004, ApJ, 609, 261
Hartmann, L. 2009, in "Protostellar Jets in Context", K. Tsinganos, T.P. Ray, M. Stute (Eds.), Springer-Verlag Berlin Heidelberg
Jensen, E. L. N., Koerner, D. W., Mathieu, R. D. 1996, AJ, 111, 2431
Lavalley-Fouquet, C., Cabrit, S., Dougados, C. 2000, A & A, 356, L41
Lay, O. P., Carlstrom, J. E., Hills, R. E. 1997, ApJ, 489, 917
Livio, M. 2009, in "Protostellar Jets in Context", K. Tsinganos, T.P. Ray, M. Stute (Eds.), Springer-Verlag Berlin Heidelberg
Matsakos, T., Tsinganos, K., Vlahakis, N., Massaglia, S., Mignone, A., Trussoni, E. 2008, A & A, 477, 521, M08
Matsakos, T., Massaglia, S., Trussoni, E., Tsinganos, K., Vlahakis, N., Sauty, C., Mignone, A. 2009, A & A, 502, 217
Mignone, A., Bodo, G., Massaglia, S., et al. 2007, ApJS, 170, 228
Najita, J. R., Carr, J. S., Glassgold, A. E., Valenti, J. A. 2007, in: "Protostars and Planets V", Reipurth, B. Jewitt, D., Keil, K. (eds.), pp. 507–522. University of Arizona Press, Tucson (2007)
Prato, L., Simon, M., Mazeh, T., et al. 2002, ApJ, 579, L99
Pyo, T.-S., Kobayashi, N., Hayashi, M., et al. 2003, ApJ, 590, 340
Ray, T. P., Mundt, R., Dyson, J. E., Falle, S. A. E. G., Raga, A. C. 1996, ApJ, 468, L103

Ray, T. P., Dougados, C., Bacciotti, F., et al. 2007, in: "Protostars and Planets V", Reipurth, B. Jewitt, D., Keil, K. (eds.), pp. 231–244. University of Arizona Press, Tucson (2007)
Stute, M., Tsinganos, K., Vlahakis, N., Matsakos, T., Gracia, J. 2008, A & A, 491, 339
Stute, M., Gracia, J., Tsinganos, K., Vlahakis, N. 2010, A & A, 516, A6, paper I
Vlahakis, N., Tsinganos, K. 1998, MNRAS, 298, 777
Vlahakis, N., Tsinganos, K., Sauty, C., Trussoni, E. 2000, MNRAS, 318, 417, V00
Woitas, J., Ray, T.P., Bacciotti, F., Davis, C.J., Eislöffel, J. 2002, ApJ, 580, 336
Zanni, C., Ferrari, A., Rosner, R., Bodo, G., Massaglia, S. 2007, A & A, 469, 811

Appendix A: Extracted line widths for all models and runs

Here we present the extracted line widths derived from synthetic [OI] λ6300 images for all models, runs and inclinations for the sake of completeness.

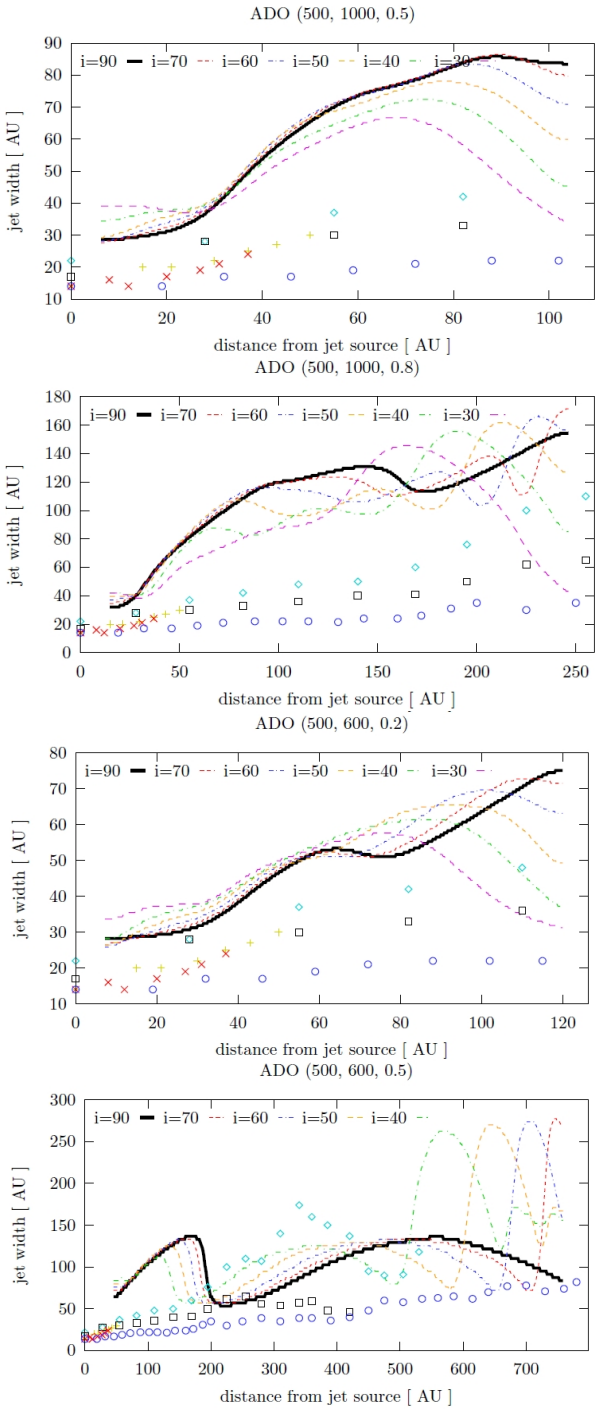

Fig. A.1. Jet widths in AU derived from synthetic [OI] images as a function of distance from the source in model ADO and for runs (500,600,0.2), (500,600,0.5), (500,1000,0.5), (500,1000,0.8); overlaid are the data points of Fig. 1.

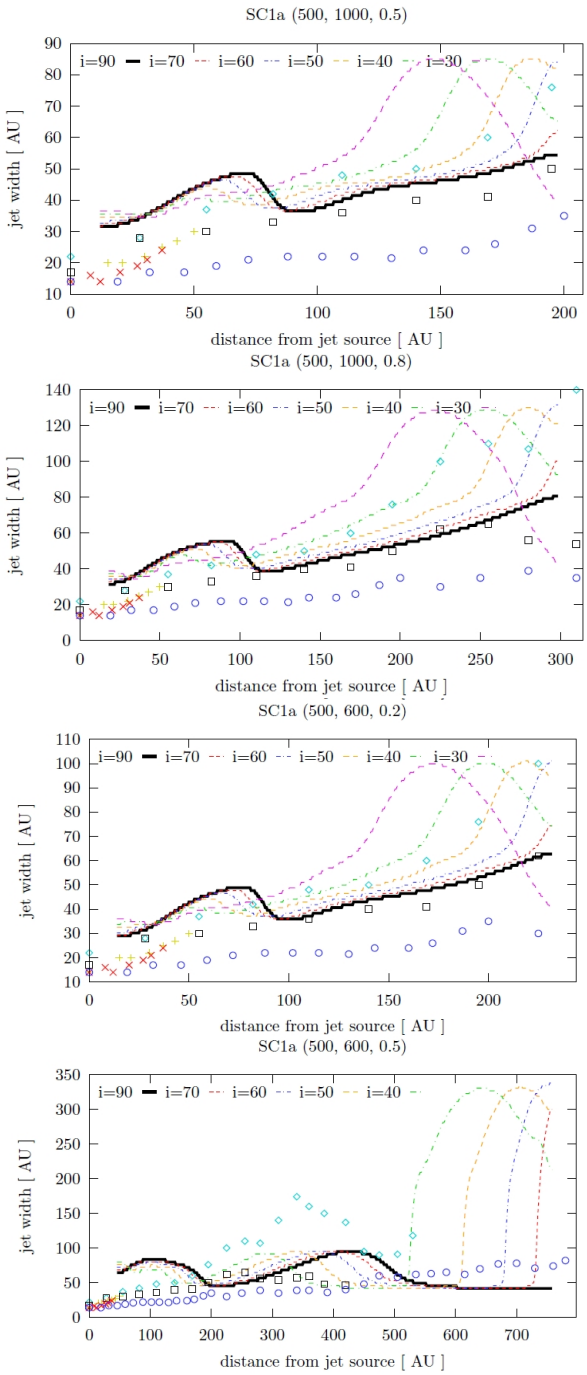

Fig. A.2. same as Fig. A.1, but in model SC1a.

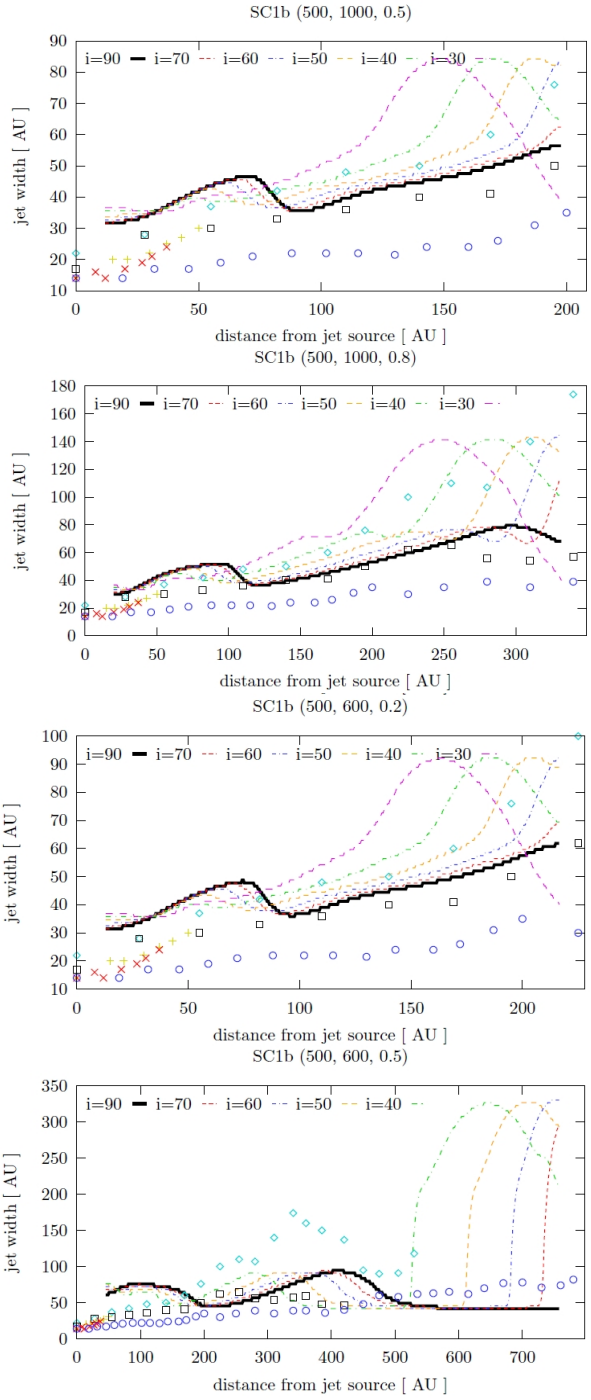

Fig. A.3. same as Fig. A.1, but in model SC1b.

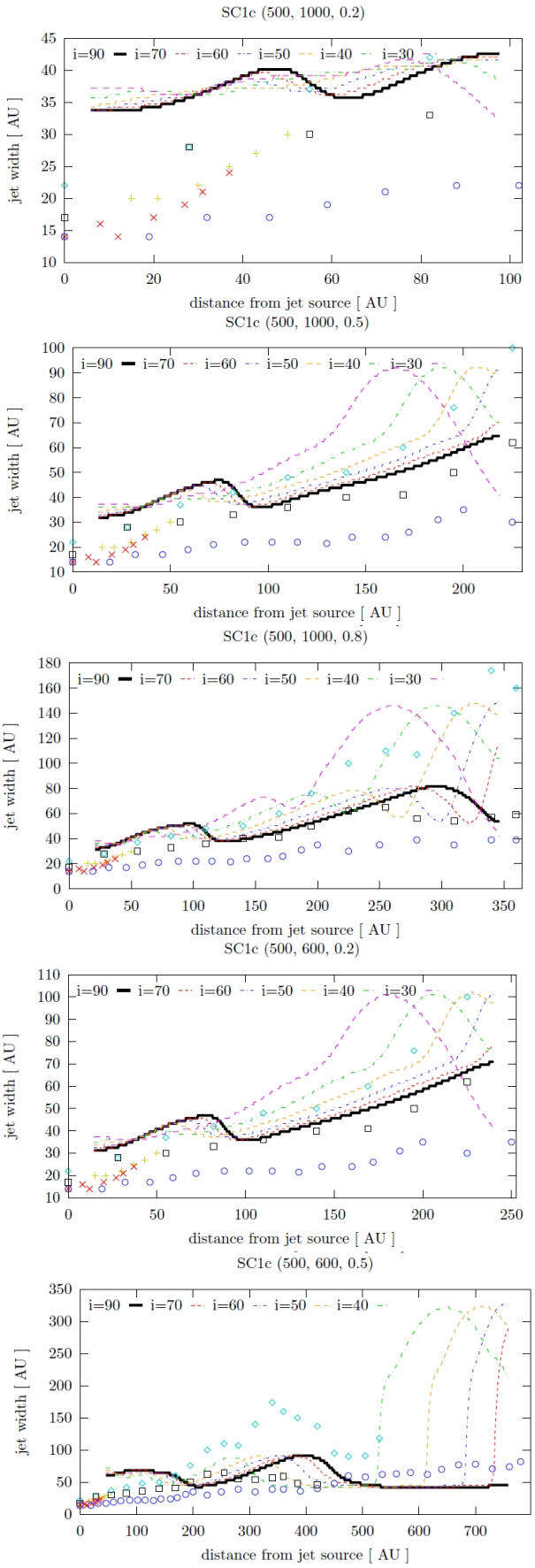

Fig. A.4. same as Fig. A.1, but in model SC1c.

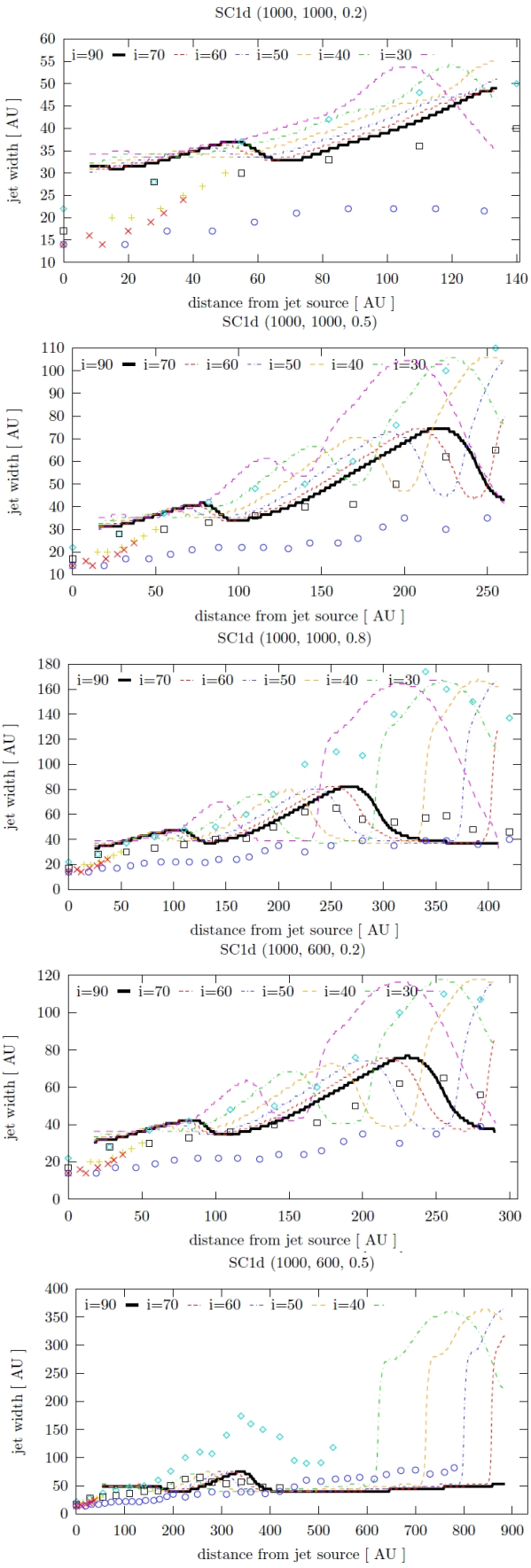

Fig. A.5. same as Fig. A.1, but in model SC1d.

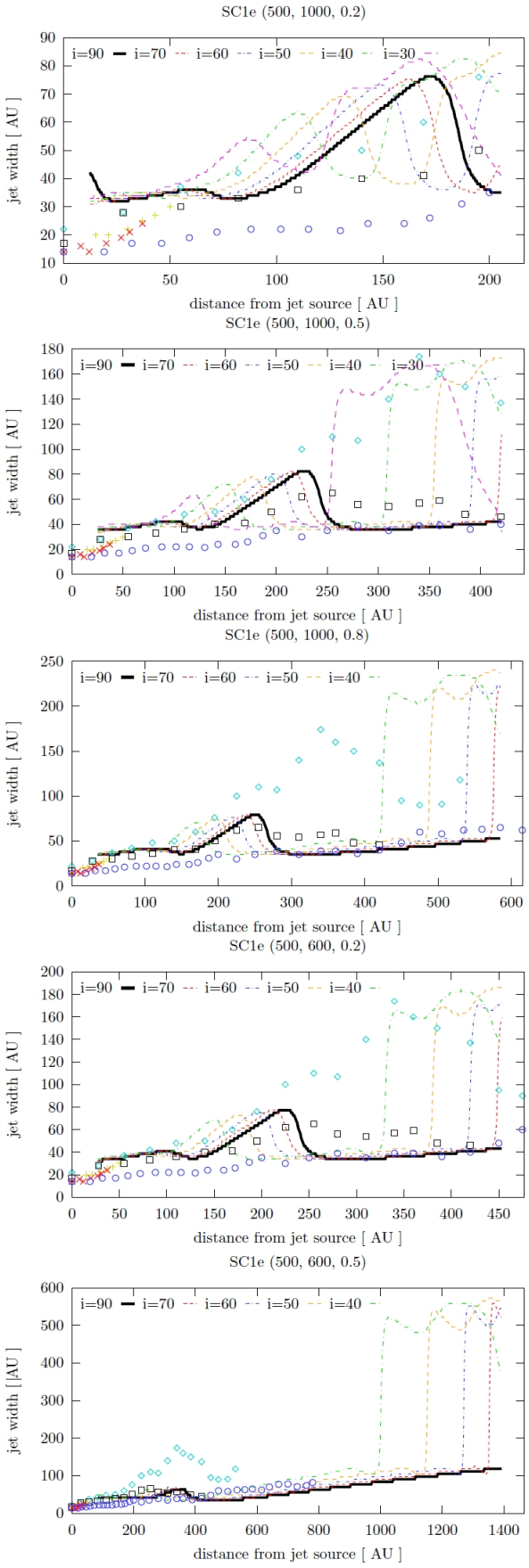

Fig. A.6. same as Fig. A.1, but in model SC1e.

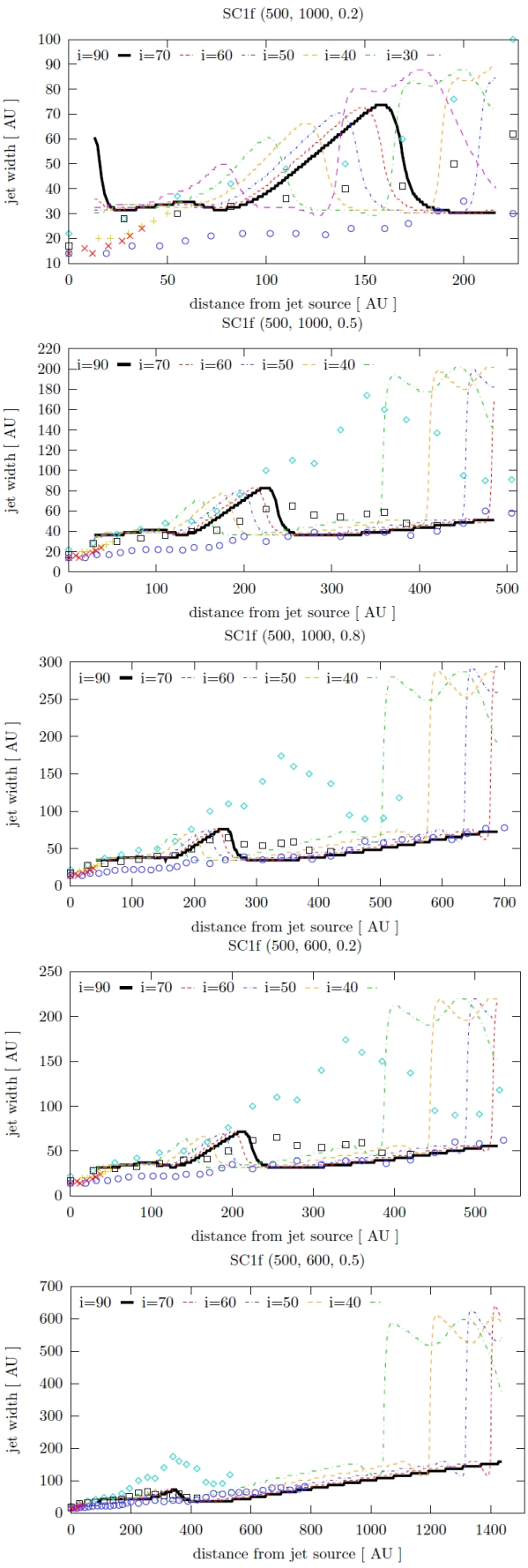

Fig. A.7. same as Fig. A.1, but in model SC1f.

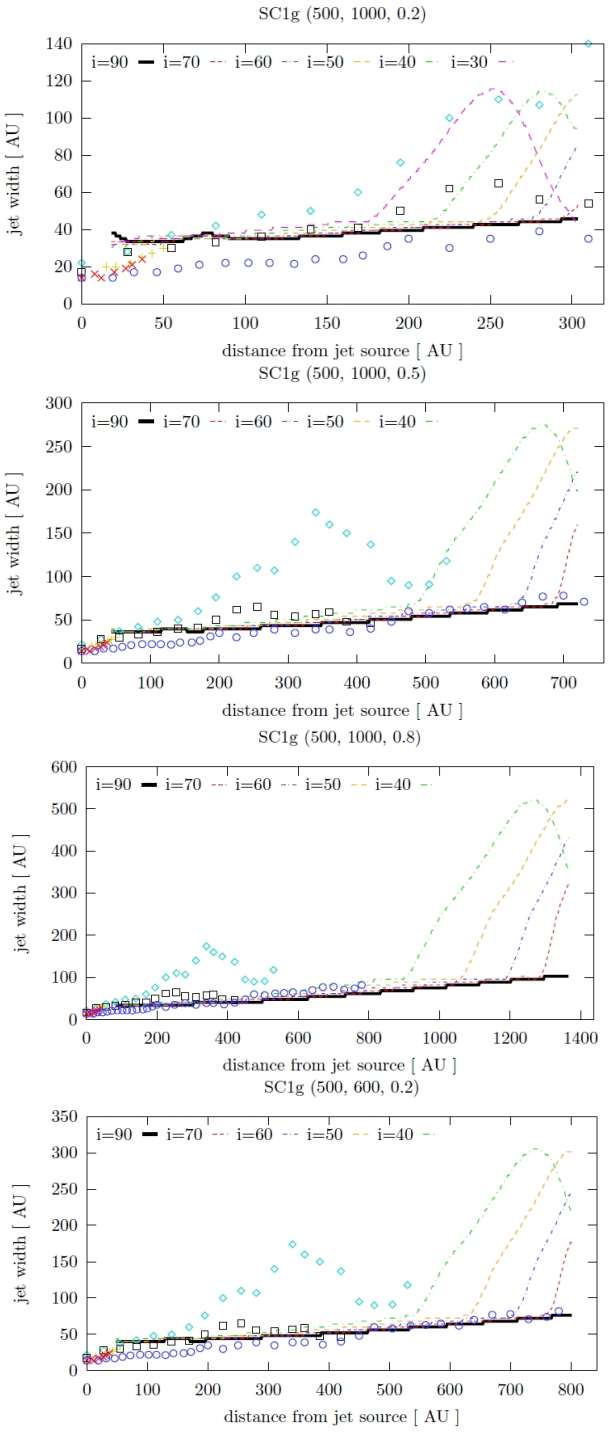

Fig. A.8. same as Fig. A.1, but in model SC1g.

Appendix B: Velocities of the jet derived from the synthetic position-velocity diagrams

model	$v_{\rm jet}$	M	inclination	$v_{\rm jet,PV}$
ADO	600	0.2	10	140
ADO	600	0.2	20	130
ADO	600	0.2	30	120
ADO	600	0.2	40	73
ADO	600	0.2	50	68
ADO	600	0.2	60	58
ADO	600	0.2	70	47
ADO	600	0.2	80	32
ADO	600	0.2	90	0
ADO	600	0.5	10	527
ADO	600	0.5	20	396
ADO	600	0.5	30	375
ADO	600	0.5	40	302
ADO	600	0.5	50	172
ADO	600	0.5	60	99
ADO	600	0.5	70	52
ADO	600	0.5	80	16
ADO	600	0.5	90	0
ADO	1000	0.5	10	120
ADO	1000	0.5	20	99
ADO	1000	0.5	30	99
ADO	1000	0.5	40	89
ADO	1000	0.5	50	99
ADO	1000	0.5	60	94
ADO	1000	0.5	70	83
ADO	1000	0.5	80	37
ADO	1000	0.5	90	0
ADO	1000	0.8	10	141
ADO	1000	0.8	20	141
ADO	1000	0.8	30	130
ADO	1000	0.8	40	130
ADO	1000	0.8	50	130
ADO	1000	0.8	60	109
ADO	1000	0.8	70	78
ADO	1000	0.8	80	37
ADO	1000	0.8	90	0

model	$v_{\rm jet}$	M	inclination	$v_{\rm jet,PV}$
SC1a	600	0.2	10	193
SC1a	600	0.2	20	198
SC1a	600	0.2	30	167
SC1a	600	0.2	40	115
SC1a	600	0.2	50	58
SC1a	600	0.2	60	42
SC1a	600	0.2	70	63
SC1a	600	0.2	80	42
SC1a	600	0.2	90	0
SC1a	600	0.5	10	760
SC1a	600	0.5	20	500
SC1a	600	0.5	30	271
SC1a	600	0.5	40	89
SC1a	600	0.5	50	37
SC1a	600	0.5	60	99
SC1a	600	0.5	70	104
SC1a	600	0.5	80	73
SC1a	600	0.5	90	0
SC1a	1000	0.5	10	230
SC1a	1000	0.5	20	276
SC1a	1000	0.5	30	260
SC1a	1000	0.5	40	183
SC1a	1000	0.5	50	109
SC1a	1000	0.5	60	68
SC1a	1000	0.5	70	94
SC1a	1000	0.5	80	32
SC1a	1000	0.5	90	0
SC1a	1000	0.8	10	433
SC1a	1000	0.8	20	520
SC1a	1000	0.8	30	401
SC1a	1000	0.8	40	220
SC1a	1000	0.8	50	63
SC1a	1000	0.8	60	94
SC1a	1000	0.8	70	58
SC1a	1000	0.8	80	47
SC1a	1000	0.8	90	0

model	$v_{\rm jet}$	M	inclination	$v_{\rm jet,PV}$
SC1b	600	0.2	10	198
SC1b	600	0.2	20	198
SC1b	600	0.2	30	183
SC1b	600	0.2	40	115
SC1b	600	0.2	50	68
SC1b	600	0.2	60	32
SC1b	600	0.2	70	78
SC1b	600	0.2	80	52
SC1b	600	0.2	90	0
SC1b	600	0.5	10	780
SC1b	600	0.5	20	505
SC1b	600	0.5	30	276
SC1b	600	0.5	40	89
SC1b	600	0.5	50	42
SC1b	600	0.5	60	94
SC1b	600	0.5	70	109
SC1b	600	0.5	80	68
SC1b	600	0.5	90	0
SC1b	1000	0.5	10	328
SC1b	1000	0.5	20	286
SC1b	1000	0.5	30	244
SC1b	1000	0.5	40	177
SC1b	1000	0.5	50	120
SC1b	1000	0.5	60	73
SC1b	1000	0.5	70	68
SC1b	1000	0.5	80	63
SC1b	1000	0.5	90	0
SC1b	1000	0.8	10	469
SC1b	1000	0.8	20	497
SC1b	1000	0.8	30	406
SC1b	1000	0.8	40	198
SC1b	1000	0.8	50	78
SC1b	1000	0.8	60	68
SC1b	1000	0.8	70	63
SC1b	1000	0.8	80	36
SC1b	1000	0.8	90	0

model	$v_{\rm jet}$	M	inclination	$v_{\rm jet,PV}$
SC1c	600	0.2	10	236
SC1c	600	0.2	20	224
SC1c	600	0.2	30	177
SC1c	600	0.2	40	121
SC1c	600	0.2	50	68
SC1c	600	0.2	60	32
SC1c	600	0.2	70	73
SC1c	600	0.2	80	52
SC1c	600	0.2	90	0
SC1c	600	0.5	10	770
SC1c	600	0.5	20	521
SC1c	600	0.5	30	286
SC1c	600	0.5	40	110
SC1c	600	0.5	50	33
SC1c	600	0.5	60	94
SC1c	600	0.5	70	104
SC1c	600	0.5	80	68
SC1c	600	0.5	90	0
SC1c	1000	0.5	10	375
SC1c	1000	0.5	20	307
SC1c	1000	0.5	30	259
SC1c	1000	0.5	40	193
SC1c	1000	0.5	50	115
SC1c	1000	0.5	60	68
SC1c	1000	0.5	70	94
SC1c	1000	0.5	80	58
SC1c	1000	0.5	90	0
SC1c	1000	0.8	10	479
SC1c	1000	0.8	20	479
SC1c	1000	0.8	30	443
SC1c	1000	0.8	40	208
SC1c	1000	0.8	50	74
SC1c	1000	0.8	60	68
SC1c	1000	0.8	70	84
SC1c	1000	0.8	80	73
SC1c	1000	0.8	90	0

model	$v_{\rm jet}$	M	inclination	$v_{\rm jet,PV}$
SC1d	600	0.2	10	339
SC1d	600	0.2	20	261
SC1d	600	0.2	30	183
SC1d	600	0.2	40	183
SC1d	600	0.2	50	99
SC1d	600	0.2	60	43
SC1d	600	0.2	70	67
SC1d	600	0.2	80	52
SC1d	600	0.2	90	0
SC1d	600	0.5	10	744
SC1d	600	0.5	20	516
SC1d	600	0.5	30	307
SC1d	600	0.5	40	135
SC1d	600	0.5	50	26
SC1d	600	0.5	60	84
SC1d	600	0.5	70	89
SC1d	600	0.5	80	58
SC1d	600	0.5	90	0
SC1d	1000	0.5	10	485
SC1d	1000	0.5	20	401
SC1d	1000	0.5	30	260
SC1d	1000	0.5	40	188
SC1d	1000	0.5	50	125
SC1d	1000	0.5	60	78
SC1d	1000	0.5	70	83
SC1d	1000	0.5	80	47
SC1d	1000	0.5	90	0
SC1d	1000	0.8	10	594
SC1d	1000	0.8	20	453
SC1d	1000	0.8	30	432
SC1d	1000	0.8	40	250
SC1d	1000	0.8	50	104
SC1d	1000	0.8	60	115
SC1d	1000	0.8	70	130
SC1d	1000	0.8	80	94
SC1d	1000	0.8	90	0